Journal Pre-proof

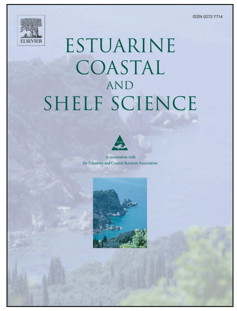

Tidal Current Characteristics in the Northern Offshore Area of the Yellow River Estuary observed by High-Frequency Surface Wave Radar

Tengfei Fu, Xinyu Guo, Yucheng Wang, Tao Zou, Fangguo Zhai, Xiaojie Yu

PII: S0272-7714(26)00384-7

DOI: https://doi.org/10.1016/j.ecss.2026.110084

Reference: YECSS 110084

To appear in: *Estuarine, Coastal and Shelf Science*

Received Date: 18 January 2026

Revised Date: 25 June 2026

Accepted Date: 25 June 2026

Please cite this article as: Fu, T., Guo, X., Wang, Y., Zou, T., Zhai, F., Yu, X., Tidal Current Characteristics in the Northern Offshore Area of the Yellow River Estuary observed by High-Frequency Surface Wave Radar, *Estuarine, Coastal and Shelf Science*, https://doi.org/10.1016/j.ecss.2026.110084.

Tidal Current Characteristics in the Northern Offshore Area of the Yellow River Estuary observed by High-Frequency Surface Wave Radar

Tengfei Fu[a,b], Xinyu Guo[c], Yucheng Wang[d], Tao Zou[e], Fangguo Zhai[f], Xiaojie Yu[a,b,*]

[a] Key Laboratory of Marine Environment and Ecology, College of Environmental Science and Engineering, Ocean University of China, Ministry of Education, Qingdao 266100, China

[b] Laboratory for Marine Ecology and Environmental Science, Qingdao Marine Science and Technology Center, Qingdao 266237, China

[c] Center for Marine Environmental Studies, Ehime University, Matsuyama 790-8577, Japan

[d] Laoshan Laboratory, Qingdao 266237, China

[e] Key Laboratory of Coastal Zone Environmental Processes and Ecological Remediation, Yantai Institute of Coastal Zone Research, Chinese Academy of Sciences, Yantai 264003, China

[f] College of Oceanic and Atmospheric Sciences, Ocean University of China, Qingdao 266100, China

Abstract: Conventional point-based measurements are inadequate for capturing the spatial variability, seasonal evolution, and debated tidal ellipticity of currents in the hydrodynamically complex Yellow River estuary. This study employed two high-frequency surface wave radar systems to acquire high spatio-temporal resolution surface-current data in the northern Yellow River estuary from April to September 2021. Through spectral and harmonic analysis, we examined the characteristics of tidal currents and their seasonal variations. The results indicate that the area is predominantly influenced by semidiurnal tides, with M_2 constituent as the principal component. We identified two regions with enhanced M_2 velocities exceeding 50 cm/s: one near Shenxiangou, which is adjacent to an M_2 amphidromic point, and another near the Yellow River estuary. Notably, radar observations revealed a predominance of rotational flow near the estuary, a pattern that diverges from the bidirectional flow typically described by conventional models. Besides, during the observation period, both the M_2 amplitude and the intensity of clockwise rotational flow increased in July. We further investigated these intensifications using river discharge records and CTD profiles, identifying water-column stratification as the primary driver. Near the estuary, enhanced summer stratification results primarily from the vertical salinity gradients induced by increased river discharge; near Shenxiangou, it is influenced by both temperature and salinity gradients, with salinity exerting a more substantial effect. Collectively, these results demonstrate that high-frequency radar observations provide critical insights into the dynamic processes in a rapidly evolving estuarine environment. It offers a novel mechanistic understanding of how river discharge and stratification regulate coastal tidal flows.

Key words: radar observations, river plume area, tidal current, seasonal hydrodynamics, water column stratification

1. Introduction

Tidal currents represent one of the most significant physical processes in coastal waters and have been extensively studied through long-term field observations, satellite altimetry data, and numerical modeling (Guo and Yanagi, 1998; Cancet et al., 2019; Zaron and Elipot, 2024). In open ocean, the velocity and direction of tidal currents vary temporally, often exhibiting rotary flow patterns. Nearshore, tidal currents are typically influenced by local bathymetry and tend to manifest as reciprocating flows (Hsu et al., 2021). As a fundamental aspect of oceanographic research, tidal currents affect the transport of pollutants (Prandle, 1997), sediment dynamics (Wiseman et al., 1986; Bi et al., 2010), and the morphological evolution of coastlines (Zhang et al., 2023).

A variety of instruments are employed to observe tidal currents, including current meters, Acoustic Doppler Current Profilers (ADCPs), drifting buoys, and satellite remote sensing technologies. However, each of these methods has inherent limitations. Due to significant spatial variability, tidal currents are more complex than water levels. Buoys and ADCPs typically provide velocity time series at discrete locations, limiting their capacity to capture flow data over extensive marine areas. Satellite altimeters and Synthetic Aperture Radar (SAR) systems offer broader spatial coverage but at the expense of reduced accuracy and sensitivity to weather conditions (Shen et al., 2013; Wang et al., 2025). In contrast, High-Frequency Surface Wave Radar (HFSWR) presents several advantages, including high temporal and spatial resolution, wide coverage, ease of operation, minimal weather dependency, and low operational costs. Consequently, HFSWR has been widely applied in nearshore surface current observations and effectively addresses the gaps left by other observational techniques in coastal regions (Lipa et al., 1990; Paduan and Washburn, 2013; Wang et al., 2020).

HFSWR possesses the capability to continuously acquire extensive, long-duration data on ocean currents, which has led to its widespread application in the study of tidal currents in many coastal areas (Paduan and Washburn, 2013). For instance, Lai et al. (2017) employed a dual-radar system to analyze the characteristics and classifications of tidal currents in the Taiwan Strait. Mandal (2024) utilized HFSWR to validate the seasonal surface currents in the Gulf of Cambay, India, and to elucidate the spatio-temporal variability of the M_2 tidal constituent. Lee et al. (2013) investigated the response patterns of bay-type estuarine tides along the western coast of Korea to wind fields and freshwater inputs. Additionally, Wang et al. (2021) quantified the tidal current features in the Taiwan Strait based on HFSWR data and clarified the regulatory mechanisms of wind and topography on surface flows. Collectively, these studies underscore the unique value of HFSWR in resolving complex tidal dynamic processes in the coastal areas.

The tides in the coastal waters of China are primarily from the northwestern Pacific Ocean (Figure 1a). Upon entering the Bohai Sea, two amphidromic points of the M_2 tidal constituent are formed near Qinhuangdao and Shenxiangou (positions in Figure 1b). Extending eastward from Shenxiangou to the eastern side of the Yellow River Estuary, the tidal regime transitions sequentially from a regular diurnal tide to an irregular diurnal tide, then to an irregular semidiurnal tide, and finally to a regular semidiurnal tide (Gao et al., 2016). However, the tidal currents in the northern offshore area of the Yellow River estuary predominantly exhibit a regular semidiurnal pattern. The different tide and tidal current types in the northern offshore area of the Yellow River estuary endow this region with inherently complex hydrodynamic conditions. Furthermore, the region is subject to erosion at Shenxiangou and sediment deposition at the Yellow River estuary, which induces significant temporal variations in its hydrodynamic condition (Wang et al., 2015). The M_2 tidal constituent is the dominant component governing tidal currents in this area, and current velocities increase in association with the protrusion of the Yellow River estuary (Wang et al., 2015). Near the Yellow River estuary, the tidal currents are rectilinear and parallel to the coastline, flowing southeastward during flood tide and northwestward during ebb tide, with maximum velocities reaching 0.5 to 1 m/s (Bi et al., 2010; Gao et al., 2016). However, constrained by observational methods, there is a paucity of observational studies in this region, and numerical models often suffer from inaccuracies in coastal bathymetric parameters (Wang et al., 2024). Therefore, the analysis of high-resolution, large-scale observational tidal current data near the Yellow River estuary is of significant importance for enhancing the understanding of tidal dynamics in the northern estuarine waters.

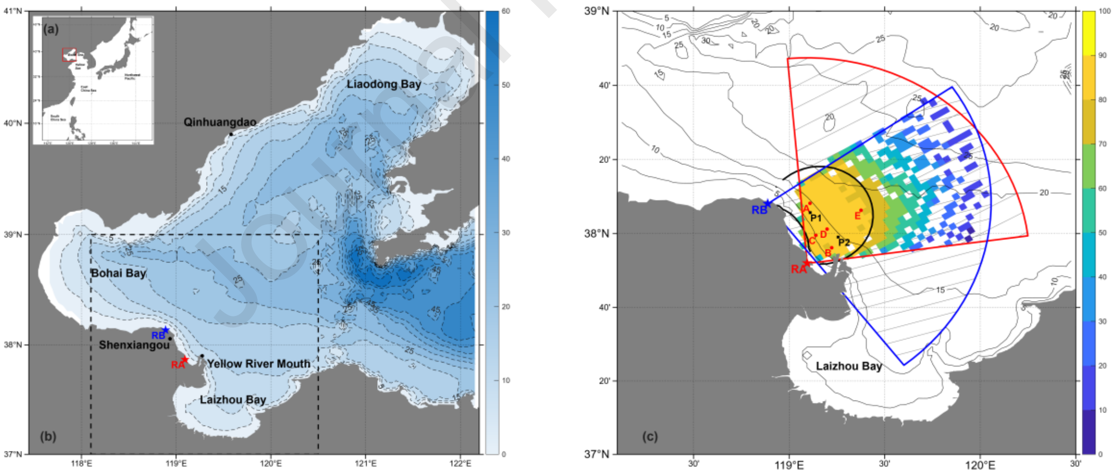

Figure 1. (a) Geographic map of the Northwest Pacific Ocean region. The red rectangle outlines the area shown in (b). (b) Bohai Sea region and water depth (m, color). Black dots in the figure denote the locations of the Yellow River Mouth, Shenxiangou, and Qinhuangdao. The red and blue pentagrams represent the HFSWR stations at Gudong (RA) and Zhuangxi (RB), respectively. The black dashed rectangle indicates the area enlarged in (c). (c) Radar data coverage area (color) in the northern part of

the Yellow River estuary, expressed as a percentage. Black contour lines indicate water depth contours (m). The solid red and blue lines denote the high-precision observation areas of the HFSWR stations at Gudong (RA) and Zhuangxi (RB), respectively. The black solid line encloses the area where GDOP ≤ 2. The final data used in our analysis are those points within the ranges enclosed by the red, blue, and black lines with ≥60% coverage rate of valid radar radial velocities. The positions of the five grid points used for data analysis are marked with red dots, labeled A to E. Black squares mark points P1 and P2, where in-situ observation data (e.g., temperature, salinity, and density) were obtained.

Tidal currents in shallow coastal waters exhibit seasonal variability due to changes in stratification (Xing and Davies, 1998). In the northern region of the Yellow River estuary, thermal stratification typically emerges in early April, reaches its peak intensity by mid-July, and persists until late September (Huang et al., 1999). Beyond thermal stratification, the northern Yellow River estuary is significantly influenced by freshwater discharge from the Yellow River (Yu et al., 2021). Simulations by Wang et al. (2008) indicate that the halocline strengthens progressively during spring and attains its maximum intensity in summer. Observations in Yu et al. (2021) before and after Water-Sediment Regulation Scheme (WSRS) in the Yellow River reveal that prior to WSRS, when river discharge was relatively low, freshwater was distributed upstream and vertical salinity profiles were nearly uniform. However, during and after the WSRS, pronounced stratification developed near the estuary. To comprehensively understand how tidal currents near the Yellow River estuary vary over different temporal scales under the influence of density stratification, extensive observational data covering a large spatial domain are required for further analysis.

Previous investigations of the Yellow River mouth region were mostly based on point-scale measurements, which cannot capture the spatial distribution of tidal currents. In particular, the ellipticity of tidal currents near the river mouth has remained controversial. In many typical estuaries, it is well documented that freshwater input and the resulting stratification can induce rotational tidal flow, with the degree of rotation increasing as river discharge strengthens (Souza and Simpson, 1996; Carbajal and Pohlmann, 2004). In the case of the Yellow River mouth, however, most earlier studies either did not consider the influence of the buoyant plume on tidal ellipses, or assumed that the flow there remained predominantly rectilinear (Gao et al., 2016; Yu et al., 2021). This disagreement has been difficult to resolve because traditional observational techniques lack the spatial coverage needed to directly capture the plume-modulated flow field, and the temporal evolution of stratification in this area has not been examined before.

To address these issues, the present study employs observed surface current fields derived from high-frequency surface wave radar, which provide synoptic, two-dimensional spatial coverage of the flow field. The first objective is to use this high-resolution mapping capability to delineate the spatial structure of tidal currents over the northern part of the Yellow River mouth area, where previous point-based observations could not resolve the detailed flow patterns. The second objective is to examine, with the aid of complementary data, whether time-varying stratification alters the tidal currents near the river mouth—specifically, whether it induces rotational rather than purely rectilinear flow and thereby influences the local tidal ellipticity.

2. Observation data and methods

The radar network utilized in this study comprised two Ocean State Monitoring and Analyzing Radar (OSMAR-S100) systems developed by Wuhan University, which were deployed at two sites:

Gudong (RA) and Zhuangxi (RB), as illustrated in Figure 1c. Initially, the observational boundaries for the two coastal radar stations—RA located at 119.094°E, 37.8672°N, and RB at 118.888°E, 38.1347°N—were defined, each with a maximum detection radius of 102.5 kilometers. However, the high-precision coverage areas were determined based on ±45° from the normal direction (Wang et al., 2020), as indicated by the red and blue solid lines in Figure 1c, representing the respective observation ranges of the RA and RB radar stations.

A grid system with a spatial resolution of 3 kilometers was established using the baseline formed by the line connecting the two stations. Geometric Dilution of Precision (GDOP) values were computed directly via the azimuth angle, thereby circumventing errors typically introduced by conventional interpolation methods. This study utilized HFSWR observation data from two stations, RA and RB, to derive hourly sea surface current fields from April 14 to September 17, 2021, employing a vector synthesis approach. By integrating the constructed grid and the GDOP data, grid points with GDOP values less than or equal to 2 were selected as valid points for the synthesis region, delineated by the black solid line in Figure 1c. This threshold was chosen based on the error analysis of Chapman et al. (1997), which demonstrated that for GDOP ≤ 2 the geometric contribution to velocity error remains sufficiently small, and such locations are considered to have good geometric coverage for reliable vector synthesis.

The polar coordinate grids of two radar stations were calculated separately: RA station comprised 40 range bins and 70 azimuth bins, while RB station included 40 range bins and 43 azimuth bins. Radar bins were spatially matched to the grid, with a threshold set at half the grid resolution to determine bin assignment. Hourly radial velocity data from both stations were read sequentially, and invalid values were removed. Subsequently, the number of valid radar observations corresponding to each grid point was tallied. For grid points with at least one valid observation from both RA and RB stations, a two-dimensional velocity vector (u, v) was synthesized using the least squares estimation method (tuvLS function). This approach prioritized spatial consistency and error control, ensuring robust flow field reconstruction within the overlapping coverage area of the dual-radar system. Spatial acquisition rate distributions over the analyzed time period were statistically evaluated, and grid points with data acquisition rates equal to or exceeding 60% were selected for extracting vector surface current data for subsequent analysis (depicted by color shading in Figure 1c). The 60% threshold was chosen to balance spatial coverage and temporal continuity, ensuring that each retained grid point possessed a sufficient number of valid hourly snapshots for reliable harmonic analysis and spectral estimation, while excluding sporadically observed locations (Kaplan et al., 2005; Shen et al., 2014; Wang et al., 2020). The final dataset used for analysis was confined to regions within the high-precision zone where the GDOP was less than or equal to 2 and the temporal coverage rate was at least 60% (areas enclosed by the red, blue, and black lines in Figure 1c).

Within the study area, five representative points (A–E) were selected for comparative analysis: points A and B near Shenxiangou and Yellow River estuary, respectively, where strong tidal currents had been reported in the literature, and points C, D, and E where there are different water depths. Rotary power spectral density estimation was performed on the complex velocity time series using Welch's method (1024-point Hanning window, 50% overlap, centered two-sided spectrum). Negative frequencies indicate clockwise rotation and positive frequencies counterclockwise. The 95% confidence intervals were computed by the pwelch routine (Chavanne et al., 2007; Wang et al., 2021).

Tidal characteristics were investigated through harmonic analysis using the T_TIDE MATLAB toolbox (Pawlowicz et al., 2002) with its default parameters. Error estimates were derived from the built-in cboot method, which generates bootstrap confidence intervals based on an uncorrelated bivariate colored noise model. The statistical significance of individual tidal constituents was evaluated using the signal-to-noise ratio (SNR), with constituents retained only if their SNR exceeded the default threshold of 2. The default Rayleigh criterion of 1 was applied to resolve constituents of similar frequency. Based on the harmonic constants (amplitudes and phase lags of the eastward and northward velocity components) of each tidal constituent obtained for each grid point, tidal ellipse parameters were further derived. For a given constituent, the superposition of two orthogonal oscillating components with a constant phase difference causes the tip of the current vector to trace an ellipse over a tidal cycle. The size, shape, orientation, and sense of rotation of this ellipse are fully determined by the two amplitudes and their phase difference. Specifically, the semi-major axis corresponds to the maximum current speed reached during the cycle, while the semi-minor axis corresponds to the minimum speed. The sign of the semi-minor axis indicates the rotation sense, with positive values denoting counter-clockwise rotation and negative values clockwise. The inclination of the ellipse is defined as the direction of the major axis, measured counter-clockwise from east and ranging from 0° to 180°. The phase of the constituent gives the timing of the maximum current.

To validate the radar-derived tidal current results, surface tidal currents were also simulated using the Princeton Ocean Model (POM; Blumberg and Mellor, 1987). The model domain covered the whole Bohai Sea with a horizontal resolution of approximately 1 km (1/90°) and 21 sigma layers in the vertical. Vertical turbulent mixing was parameterized using the level-2.5 closure scheme

(Mellor and Yamada, 1982), and horizontal eddy viscosity was represented by the Smagorinsky formulation (Smagorinsky, 1963). At the open boundary (122.38°E), four tidal constituents (M_2, S_2, K_1, O_1) were considered. The model was spun up for 365 days. The modelled tidal currents were bilinearly interpolated onto the HFSWR observation grid and underwent harmonic analysis to facilitate comparison with the HFSWR observations. This model configuration has been shown to effectively reproduce the hydrodynamic conditions near the Yellow River estuary (Yu et al., 2020; Yu et al., 2021).

To investigate whether stratification might influence the tidal currents, daily river discharge data for the Yellow River were acquired from the Lijin Hydrological Station, the last gauging station upstream of the river mouth (Figure 2a). The data cover the period from mid-April to mid-September, with discharge ranging from approximately 500 to 4000 m^3/s. The highest discharge occurred in late June to early July, followed by two additional high-discharge events in late July and early September, respectively. During the remaining periods, the discharge remained relatively low. In addition to river discharge, the sea surface wind conditions during the observation period were also obtained. They were obtained from the Cross-Calibrated Multi-Platform (CCMP) Version 2.1 RT (Near-Real-Time) gridded surface wind vector product (Level 3.0), produced and distributed by Remote Sensing Systems (RSS) (Atlas et al., 2011; Schneider et al., 2013). This product merges observations from multiple satellite scatterometers and radiometers with the NCEP GFS background field through variational analysis, yielding gridded 10-m wind vectors at a spatial resolution of 0.25° and a temporal resolution of 6 h. To represent the wind forcing over the study area, daily mean wind vectors were first computed from the 6-hourly data and then spatially averaged over the region, as the spatial variability of the wind field was relatively small. From April to May, wind speed and direction varied greatly (Figure 2b), with speed exceeding 10 m/s during northerly winds. From June to July, southeasterly winds were dominant, with speed around 5 m/s. From August to September, southerly and northeasterly winds alternated, and northeasterly winds were stronger, frequently reaching about 10 m/s.

In-situ temperature and salinity profiles around the Yellow River estuary were also acquired. They were collected during a field campaign conducted by the Yantai Institute of Coastal Zone Research, Chinese Academy of Sciences in 2022. Observations were carried out during three cruises: May 8–12, June 8–12, and July 18–22, 2022, at multiple cross-shelf sections near the Yellow River estuary (positions in Wu et al., 2025). The profiles were obtained using a Seabird SBE 911plus CTD system with a vertical resolution of 1 m, starting from 2 m depth to the sea bottom. In-situ density was obtained directly from the CTD data processed by the instrument software. Two stations, P1 (water depth ~12 m) and P2 (water depth ~14 m) (Figure 1c), located near the M_2 amphidromic point and the Yellow River estuary, respectively, were selected for analysis. These CTD data were collected in 2022 rather than during the HFSWR observation period (April–September 2021). However, because the seasonal stratification is primarily governed by solar heating and river discharge, which exhibit relatively consistent seasonal phasing, these data still provide a representative depiction of the seasonal evolution of stratification in this region.

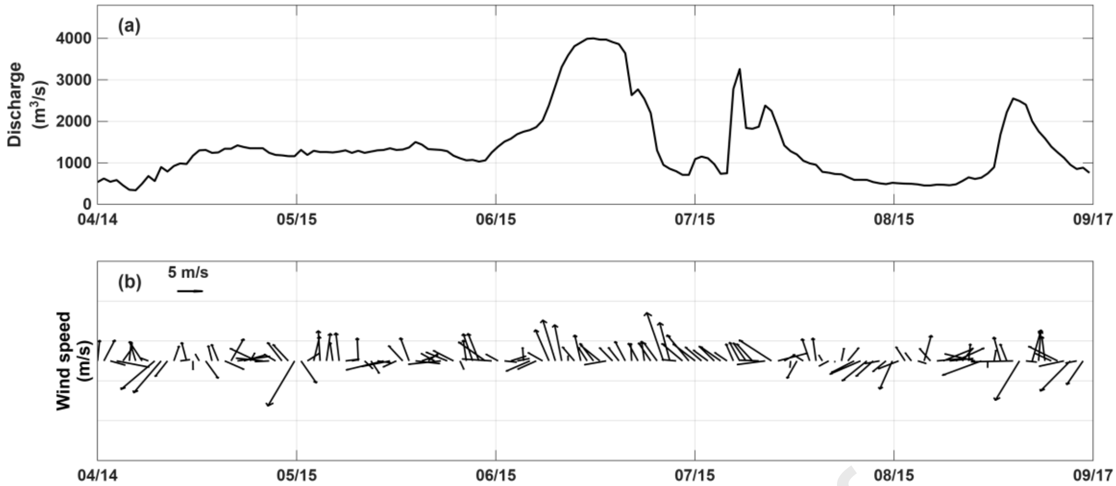

Figure 2. Time series of (a) Yellow River discharge (m^3/s) and (b) wind speed vectors (m/s) during the observation period.

3. Results

3.1 Spectral analysis of tidal current

To investigate the tidal current characteristics in the northern area of the Yellow River estuary, instantaneous surface flow maps were shown at two-hour intervals over a 12-hour period on April 29 (Figure 3), based on synthesized vector flow data. At 06:00, surface currents in the northwestern part of the region were directed eastward and southeastward, while those in the southeast flowed northeastward, both exhibiting relatively weak velocities, with a maximum speed of 55 cm/s near the estuary (Figure 3a). At 08:00, surface currents throughout the area predominantly flowed southeastward with increased intensity; most of the area experienced flow speed exceeding 50 cm/s, reaching a peak velocity of 72 cm/s offshore near Shenxiangou, and 61 cm/s near the estuary (Figure 3b). At 10:00, the surface flow remained mainly southeastward but with a clockwise deflection, with a maximum speed of 47 cm/s observed in the northern part of the region (Figure 3c). At 12:00, the currents flowed southwestward in the northeastern area and northwestward in the remaining areas with reduced velocity, peaking at 48 cm/s northeast of the estuary (Figure 3d). At 14:00, surface currents all flowed northwestward with stronger speeds, reaching a maximum of 67 cm/s offshore near Shenxiangou and 60 cm/s near the estuary (Figure 3e). At 16:00, the northwestward flow persisted also with a clockwise deflection, with a maximum velocity of 43 cm/s near the estuary (Figure 3f). At 18:00, the flow direction reversed again to southeastward with relatively weak speeds, peaking at 48 cm/s near the estuary (Figure 3g).

The surface instantaneous flows recorded at 06:00, 08:00, and 10:00 were primarily characterized by flood-tide dominance. It then transitioned to ebb-tide dominance at 12:00, 14:00, and 16:00, and reverted to flood-tide conditions at 18:00. This sequence reflects a distinct semidiurnal tidal current regime within the study region. Furthermore, as illustrated in Figure 3, the direction of tidal currents during both flood and ebb phases does not exhibit a simple linear alternation; rather, it experiences temporal deflections. This effect is especially notable near the Yellow River estuary and in the northern part of the study area.

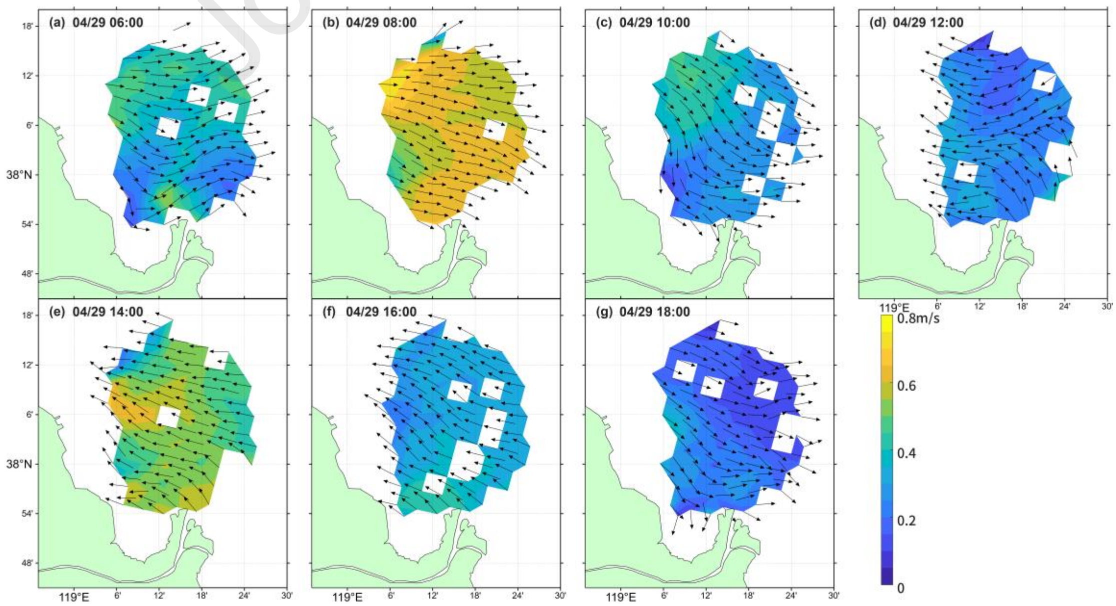

Figure 3. Instantaneous maps of surface currents at 2-hour intervals during a 12-hour period on April 29.

Color represents current speed (m/s), and arrows indicate the flow direction.

To investigate the periodic characteristics of surface currents in the northern area of Yellow River estuary, power spectral density (PSD) analyses were conducted on the time series of vector flows at five selected points (A–E, indicated by red dots in Figure 1c). The PSD plots (Figure 4) illustrated the distribution of energy across different frequency bands.

Overall, the spectra exhibited a pronounced and sharp peak within the semidiurnal frequency band (approximately ±1.8–2.2 cycles per day, cpd), indicating that semidiurnal tidal currents dominated in the study area. Notably, the clockwise component (represented by the negative half-axis) was stronger, suggesting that the semidiurnal tidal currents rotated clockwise. Within the semidiurnal signals, the M_2 constituent was significantly more prominent than the S_2 constituent in both clockwise and counterclockwise components, exceeding S_2 by 1.0 to 1.3 orders of magnitude. This finding confirmed that the semidiurnal tidal currents were primarily governed by the M_2 constituent.

The 0 cpd component, representing the relatively stable background circulation or mean flow field, showed distinct characteristics compared to periodic components such as tidal and inertial oscillations. Smaller peaks were observed near the diurnal frequency band (±0.8–1.2 cpd), where the counterclockwise component was more pronounced, indicating that diurnal tidal currents exhibited a counterclockwise rotation. Among the diurnal constituents, K_1 was slightly stronger than O_1. No distinct peak was detected at the inertial frequency (1.24 cpd at 38°N), implying that non-inertial processes predominated in this region. Additionally, minor peaks near 3 cpd and 4 cpd suggested the presence of shallow water tides; however, these were comparatively weaker than the semidiurnal and diurnal signals.

Consequently, this study primarily focused on the semidiurnal M_2 and S_2 tidal currents, as well as the diurnal K_1 and O_1 tidal constituents, given their dominant influence on the surface flow dynamics in the northern area around the Yellow River estuary.

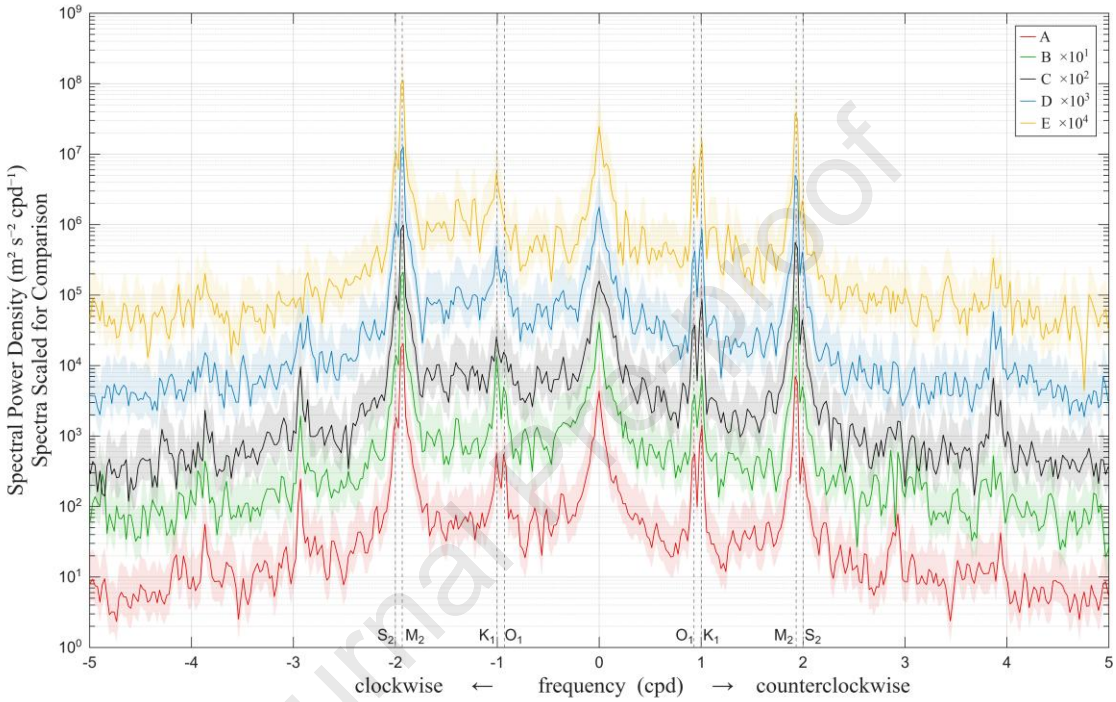

Figure 4. Bidirectional rotary spectral estimates of surface currents at points A–E. The negative and positive semi-axes represent clockwise and counter-clockwise rotating components, respectively. For clarity, curves B–E have been vertically offset by factors of 10^1, 10^2, 10^3, and 10^4, respectively, relative to curve A. Shaded regions denote the 95% confidence intervals.

3.2 Harmonic Analysis of tidal current

Harmonic analysis was conducted on the surface current at the selected grid points—specifically, those within the region enclosed by the red, blue, and black solid lines in Figure 1c. For the four principal constituents (M_2, S_2, K_1, and O_1), the tidal ellipse parameters derived from the harmonic analysis are shown in Figure 5, and the values at points A–E are summarized in Table 1.

As previously described, the tidal currents in the northern area of the Yellow River estuary were predominantly semidiurnal, with the M_2 tidal constituent representing the principal component within the radar coverage region. The major axis of the M_2 tidal current ellipses generally aligned in a northwest-southeast orientation, roughly parallel to the coastline, with the angle of inclination larger near the Yellow River estuary (Figure 5a). The rotation of the M_2 tidal current ellipses was predominantly clockwise throughout most of the area. The amplitude (defined as half the major axis of the tidal current ellipse) of the M_2 constituent ranged between 35 and 60 cm/s, exhibiting peak values near point A outside Shenxiangou and point B around the Yellow River estuary, measuring approximately 52 cm/s and 53 cm/s, respectively. The amplitude gradually decreased with increasing of water depth offshore. The spatial distribution characteristics of the S_2 tidal constituent ellipses closely resembled those of the M_2 constituent, with strong current zones located in similar positions and exhibiting the same clockwise rotation (Figure 5b). The maximum amplitude of the S_2 constituent reached 14 cm/s, approximately one-quarter to one-third of the M_2 amplitude. In contrast, the K_1 and O_1 tidal constituents displayed distribution patterns that differed markedly from the semidiurnal tides. The K_1 tidal currents exhibited lower velocities near the western shore, increasing toward the east and north (Figure 5c), while the O_1 currents showed the lowest velocities in the southwest but attained their maximum near the Yellow River estuary and the northwestern region (Figure 5d). Compared to the M_2 constituent, the K_1 and O_1 tidal currents were much weaker, with maximum velocities ranging from 4 to 12 cm/s, roughly one-sixth to one-third of the M_2 current speeds. Although the principal axes of the K_1 and O_1 tidal current ellipses were oriented similarly to those of the M₂ and S₂ constituents, the tidal current ellipses within the radar coverage area predominantly rotated counterclockwise, except near the estuary and in the northwestern region where clockwise rotation was observed.

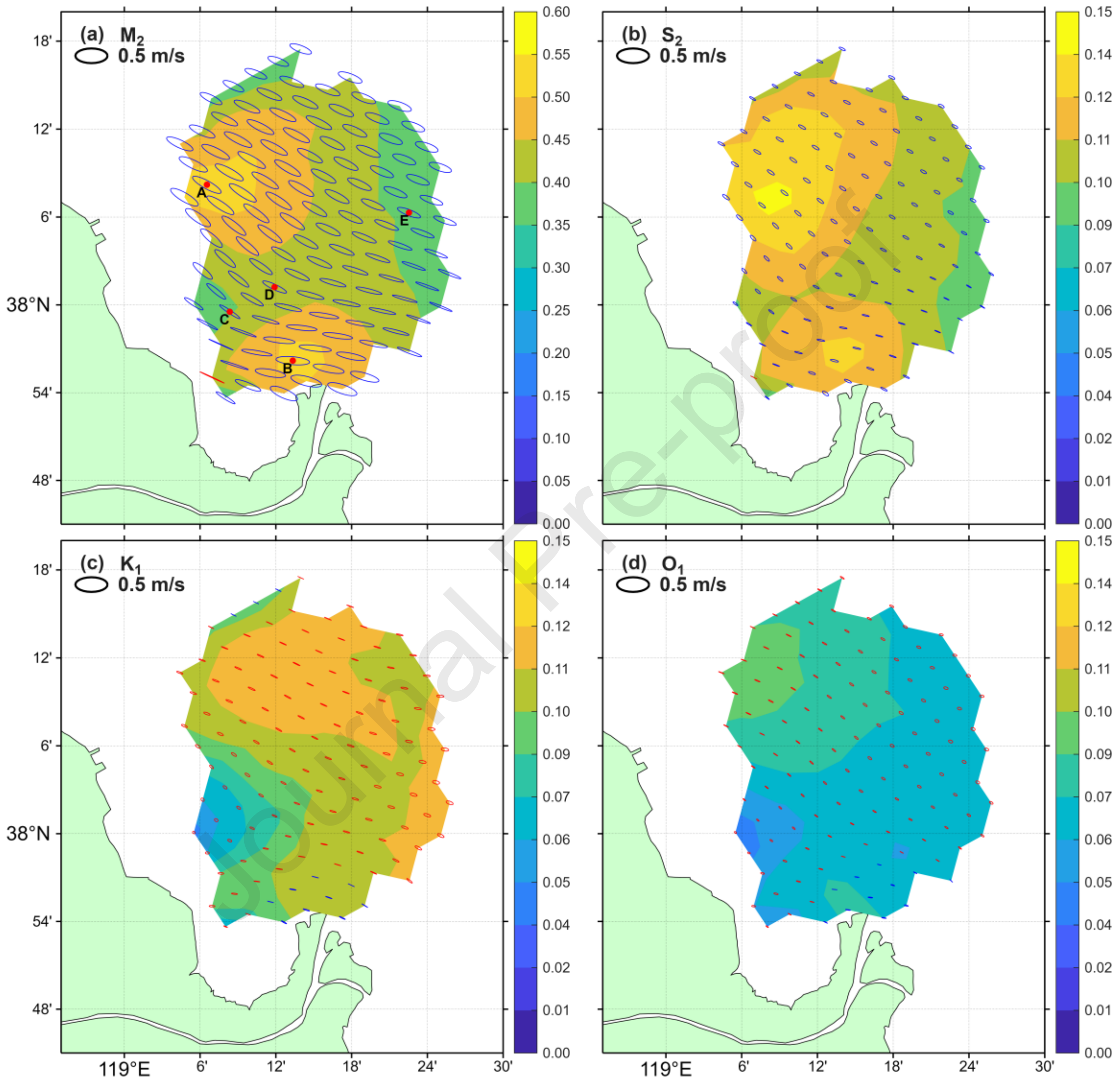

Figure 5. Distributions of tidal current ellipses (color denotes the semi-major axis, m/s) derived from HFSWR observations for the four major tidal constituents: (a) M_2, (b) S_2, (c) K_1, and (d) O_1. Blue and red ellipses indicate clockwise and counter-clockwise rotation of the tidal current vectors, respectively.

Table 1. Harmonic analysis results for Points A–E. Major is the semi-major axis of tidal current ellipse

(maximum current velocity), Minor is the semi-minor axis (minimum current velocity), Phase is the tidal constituent phase lag relative to theoretical potential, Inclination is the semi-major axis orientation (counter-clockwise from east, indicating maximum flow direction), and SNR is the signal-to-noise ratio.

Point	Name	Major (m/s)	Minor (m/s)	Phase (degree)	Inclination (degree)	SNR
A	O_1	0.09	0.01	152.60	11.35	30.89
	K_1	0.11	0.03	157.84	280.56	62.52
	M_2	0.52	-0.13	148.43	132.77	756.47
	S_2	0.14	-0.04	142.18	52.44	43.85
B	O_1	0.08	0.00	174.43	359.02	13.69
	K_1	0.10	-0.01	168.88	275.11	27.45
	M_2	0.53	-0.14	174.14	134.25	804.24
	S_2	0.13	-0.03	164.83	55.41	40.53
C	O_1	0.05	0.02	138.34	7.76	9.60
	K_1	0.07	0.04	155.71	285.75	12.81
	M_2	0.39	-0.05	143.70	133.86	366.03
	S_2	0.11	-0.02	139.39	52.20	40.18
D	O_1	0.07	0.02	140.56	7.73	15.74
	K_1	0.08	0.02	154.35	281.87	17.45
	M_2	0.42	-0.09	152.67	137.12	620.90
	S_2	0.11	-0.03	149.85	55.01	43.05
E	O_1	0.07	0.04	153.09	19.90	8.64
	K_1	0.11	0.04	168.82	290.78	26.00
	M_2	0.39	-0.10	156.79	138.23	970.09
	S_2	0.10	-0.04	149.71	58.06	47.08

To clarify whether the tidal currents in the northern area of the Yellow River estuary are rotational or rectilinear, the distributions of ellipticity of the four principal tidal constituent ellipses were shown (Figure 6). Ellipticity (k) is defined as the ratio of the minor axis to the major axis of the tidal current ellipse. When $k > 0.25$, the tidal current exhibits strong rotational behavior; conversely, when $k < 0.25$, the current is predominantly rectilinear (Guo et al., 2018). Near the estuary, the M_2 ellipticity was relatively large ($k > 0.25$), signifying rotational flow (Figure 6a). As the distance from the estuary increased, the ellipticity of M_2 decreased, and the tidal current transitioned to rectilinear flow; further offshore, the ellipticity increased again, reverting to rotational flow. Overall, bottom friction suppresses the rotational component of tidal current, favoring more rectilinear flow (i.e. low ellipticity). Near the estuary, stratification suppresses friction, so ellipticity stays high. Further offshore, friction weakens with depth, allowing ellipticity becoming larger (more details in Section 4.2). The ellipticity distribution of the S_2 constituent resembled that of M_2 but with a broader spatial extent of rotational flow, particularly in the northern half of the area (Figure 6b). In contrast, the ellipticity distributions of the diurnal constituents K_1 and O_1 differed from those of M_2 and S_2: rotational current regions were mainly located on the eastern and western sides of the study area, while rectilinear currents dominated near the estuary (Figures 6c and 6d).

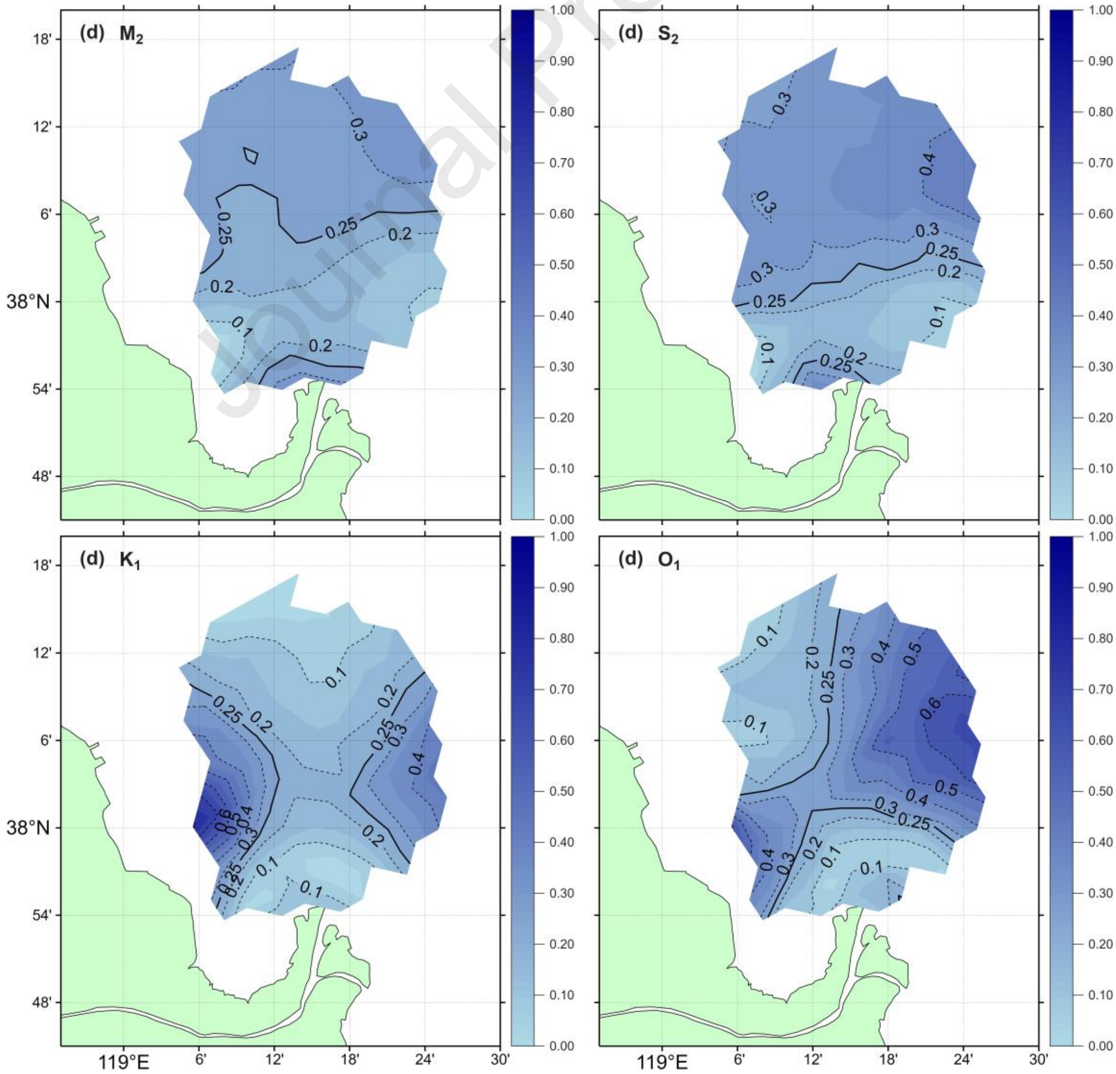

Figure 6. Distributions of tidal current ellipticity derived from HFSWR observations for (a) M_2, (b) S_2, (c) K_1, and (d) O_1.

Furthermore, we calculated tidal characteristic parameters to classify the type of tidal currents. The criterion for tidal classification is defined as follows (Shen et al., 2013):

$$F = \frac{W_{O1} + W_{K1}}{W_{M2}} \quad (1)$$

where W_{O1}, W_{K1}, W_{M2} represent the semi-major axes of the tidal ellipses corresponding to the O_1, K_1, and M_2 tidal constituents, respectively. The classification standards are: $F \leq 0.5$ indicates a regular semidiurnal tide; $0.5 < F \leq 2.0$ corresponds to an irregular semidiurnal tide; $2.0 < F \leq 4.0$ denotes an irregular diurnal tide; and $F > 4.0$ signifies a regular diurnal tide (Shen et al., 2013). The values across the region were all below 0.5 (figure not shown here), indicating that the northern Yellow River estuary was dominated by regular semidiurnal tides. Consequently, the M_2 constituent is identified as the principal tidal component.

3.3 Seasonal variations of tidal currents in the northern area of Yellow River estuary

The seasonal variations of tidal currents in the northern area of Yellow River estuary were investigated through the observational data from April 15 to September 13, 2021. The data were segmented into five consecutive 30-day periods: April 15–May 14, May 15–June 13, June 15–July 14, July 15–August 13, and August 15–September 13. Harmonic analysis was conducted for each of these periods using the four main tidal constituents (M_2, S_2, K_1, O_1), and only results of the dominant M_2 constituent are presented herein.

During all five periods, the overall characteristics of the M_2 tidal current ellipses exhibited a certain degree of similarity (Figure 7). The major axes of the tidal ellipses predominantly oriented northwest–southeast, with larger angle of inclination near the Yellow River estuary. The strongest tidal currents were observed near the outer region of Shenxiangou and in proximity to the Yellow River estuary. Amplitude decreased progressively offshore with the increase of water depth. All these characteristics showed little seasonal variations, except for the magnitude of tidal current amplitude. Compared to Period 1 (Figure 7a), Period 2 showed an amplitude increase of 6–9 cm/s in most areas, with the greatest enhancement near point D (Figure 7b). In Period 3, the most significant increase of amplitude, up to 8 cm/s, occurred near the estuary and in some northern regions, while the other areas exhibited minimal changes, with offshore amplitude variations less than 2 cm/s as compared to Period 1 (Figure 7c). Compared to Period 1, Period 4 demonstrated a pronounced amplitude increase near the estuary, exceeding 14 cm/s at its peak, and a notable increase larger than 8 cm/s in a northern zone (Figure 7d). During Period 5, three regions exhibited substantial amplitude increases as compared to Period 1: up to 13 cm/s in the northernmost area, by approximately 10–10.5 cm/s in the vicinity near point A outside Shenxiangou, and a slightly lower but still significant increase, peaking at 10 cm/s in the estuary area (Figure 7e). The maximum M_2 tidal current across all periods was recorded near the Yellow River estuary during Period 4 (61 cm/s) and near Shenxiangou during Period 5 (58 cm/s).

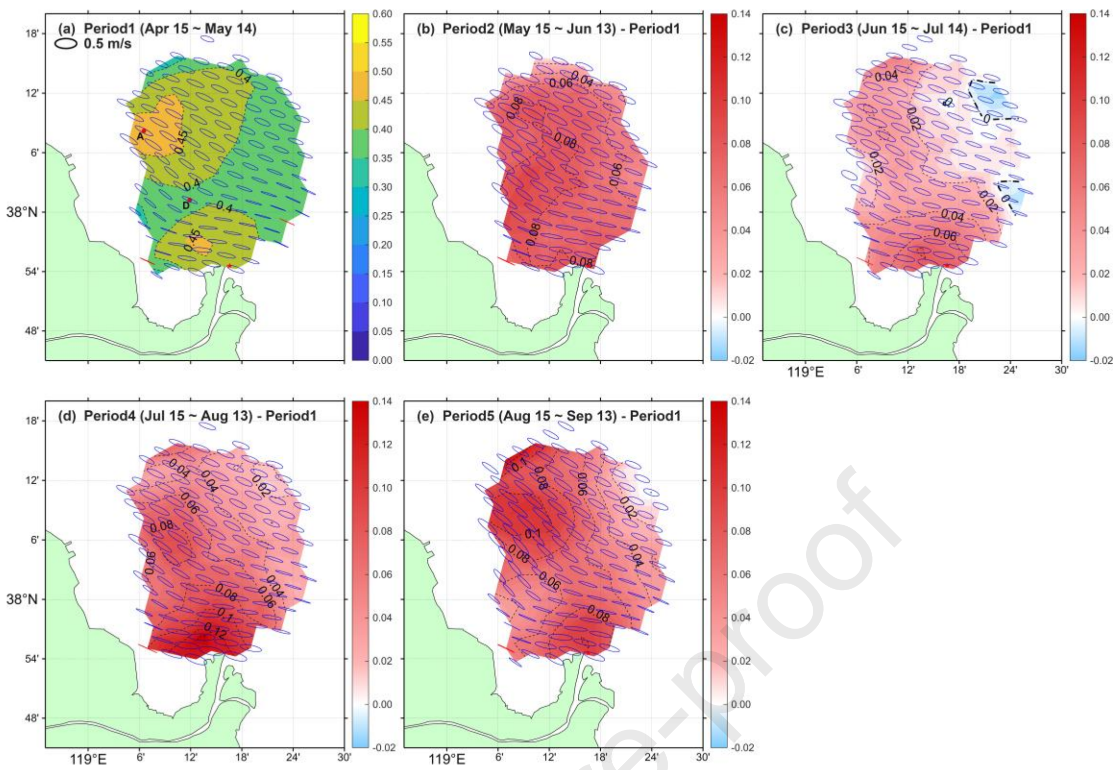

Figure 7. (a) M_2 tidal current ellipses and current amplitude (color, m/s) for Period 1; (b)–(e) M_2 tidal current ellipses and amplitude differences (color, m/s) for Periods 2–5 relative to Period 1.

Figure 8 illustrates the seasonal variation of the ellipticity of the M_2 tidal current. Among different time periods, rotational flows were consistently concentrated in the southern and northern parts of the study area. However, the values of k and the range of rotational flow regions ($k > 0.25$) exhibited seasonal variations. During Period 1 (Figure 8a), k exceeded 0.25 in the Yellow River estuary and northern offshore areas, indicating clockwise rotational flows. The other regions were dominated by $k < 0.25$, showing prominent rectilinear characteristics. Compared to Period 1, the area of clockwise rotational flows ($k > 0.25$) near the estuary in Period 2 showed little change, but the northern area expanded (Figure 8b). In Period 3 (Figure 8c), the area of clockwise rotational flows near the estuary expanded, with k values further increasing to over 0.35 at the estuary, while the rotational area further expanded in the northern area. In Period 4 (Figure 8d), the area of large k value shrank in the northwestern area as compared to Period 3, while the value in the northeast increased. The area of clockwise rotational flow near the Yellow River estuary kept large. In Period 5 (Figure 8e), the rotational area further shrank in the northern area, and the largest value became larger ($k > 0.35$) in the northeastern part, while the rotational area near the Yellow River estuary also shrank. Overall, the strongest rotationality and largest rotational area of the M_2 tidal current ellipses near the Yellow River estuary occurred during Period 3 and Period 4, and the largest rotational extent in the northern part appeared during Period 3.

As a brief summary, the amplitude of the M_2 tidal constituent exhibited pronounced seasonal variations near the outer region of Shenxiangou and Yellow River estuary. The ellipticity of the M_2 tidal current also showed the most significant seasonal variations near the Yellow River estuary and northern part of the study area.

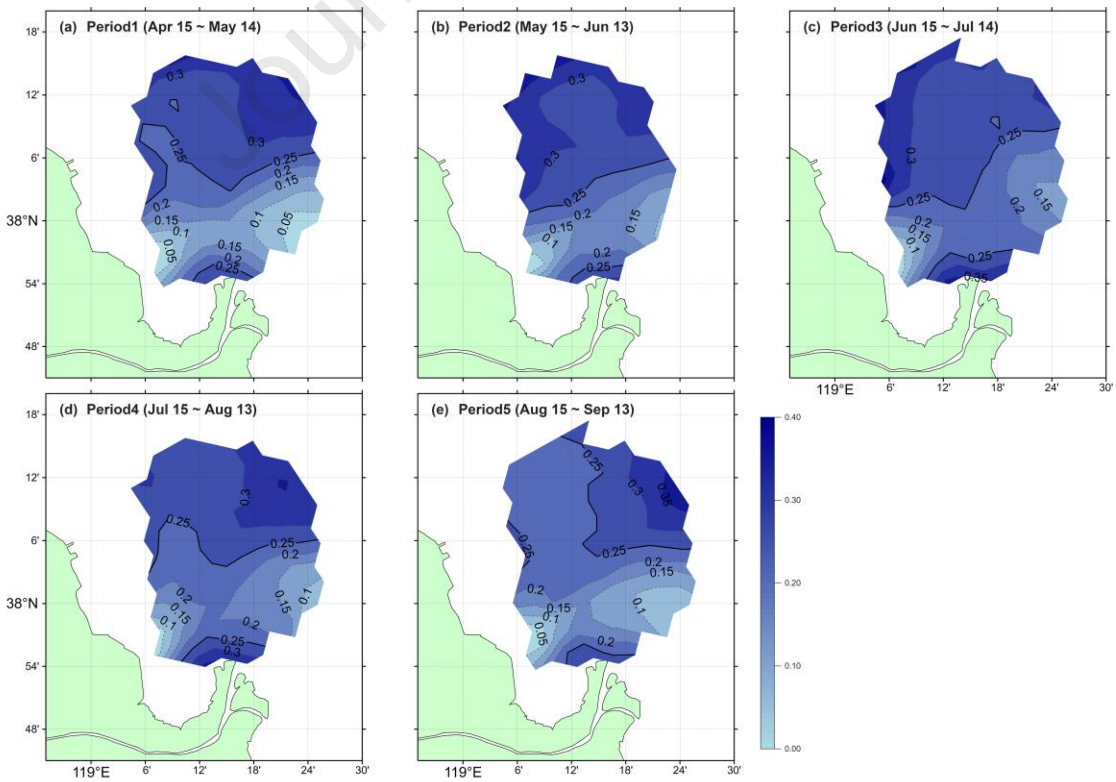

Figure 8. Distributions of M_2 tidal current ellipticity for the five periods.

4. Discussions

4.1 Comparison with previous studies on tidal current in the northern area of Yellow River estuary

Extensive research has been conducted on the characteristics of tidal currents in the areas surrounding the Yellow River estuary; however, due to limitations in observational technologies, historical tidal current data within the study region remain scarce. HFSWR represents an observational technique capable of acquiring data over large spatial extents with high temporal and spatial resolution. This section aims to evaluate, through comparison with previous observational and simulation results, whether HFSWR can effectively reveal more detailed patterns of surface tidal current in the northern area of the Yellow River estuary.

Based on field observations, Pang and Jiang (2003) identified two strong tidal current zones in the northern Yellow River estuary: one near Shenxiangou, corresponding to the M_2 amphidromic point region, and another surrounding the Yellow River estuary. However, in early simulations of tidal currents in the Bohai Sea, such as those conducted by Fang (1994), the M_2 tidal constituent amplitude in the northern Yellow River estuary generally decreases from nearshore area to offshore area. With increase of model resolution, the simulated tidal current near the Yellow River estuary has gradually aligned with observational data. Wang et al. (2015) and Gao et al. (2016) developed high-resolution models that successfully simulated the spatial structure of strong tidal current zone near the Yellow River estuary. Wang et al. (2015) further demonstrated that prior to the Yellow River's course diversion in 1996, a strong tidal current zone existed near Shenxiangou; following the diversion, a similar strong tidal current zone emerged near the Yellow River estuary. The most recent simulations by Yu et al. (2021) revealed significantly elevated M_2 tidal current velocities near Shenxiangou and the Yellow River estuary. As depicted in Section 3.2, our radar data revealed the strong tidal currents in the area near Shenxiangou and the Yellow River estuary.

A comparison of tidal ellipses between HFSWR observations and model simulations (Yu et al., 2021) is then presented in Figure 9. It showed a certain degree of consistency between radar observations and model outputs concerning semidiurnal and diurnal tides in most areas. However, the orientation of M_2 tidal ellipse derived from radar data is more westward than that of model result near the Yellow River estuary. Besides, in the area near the Yellow River estuary, the M_2 tidal ellipse derived from radar data is more circular than that by model result (Figure 9a). The larger tidal ellipticity by radar data indicated a more rotating tidal current rather than the reciprocating tidal current in the model result.

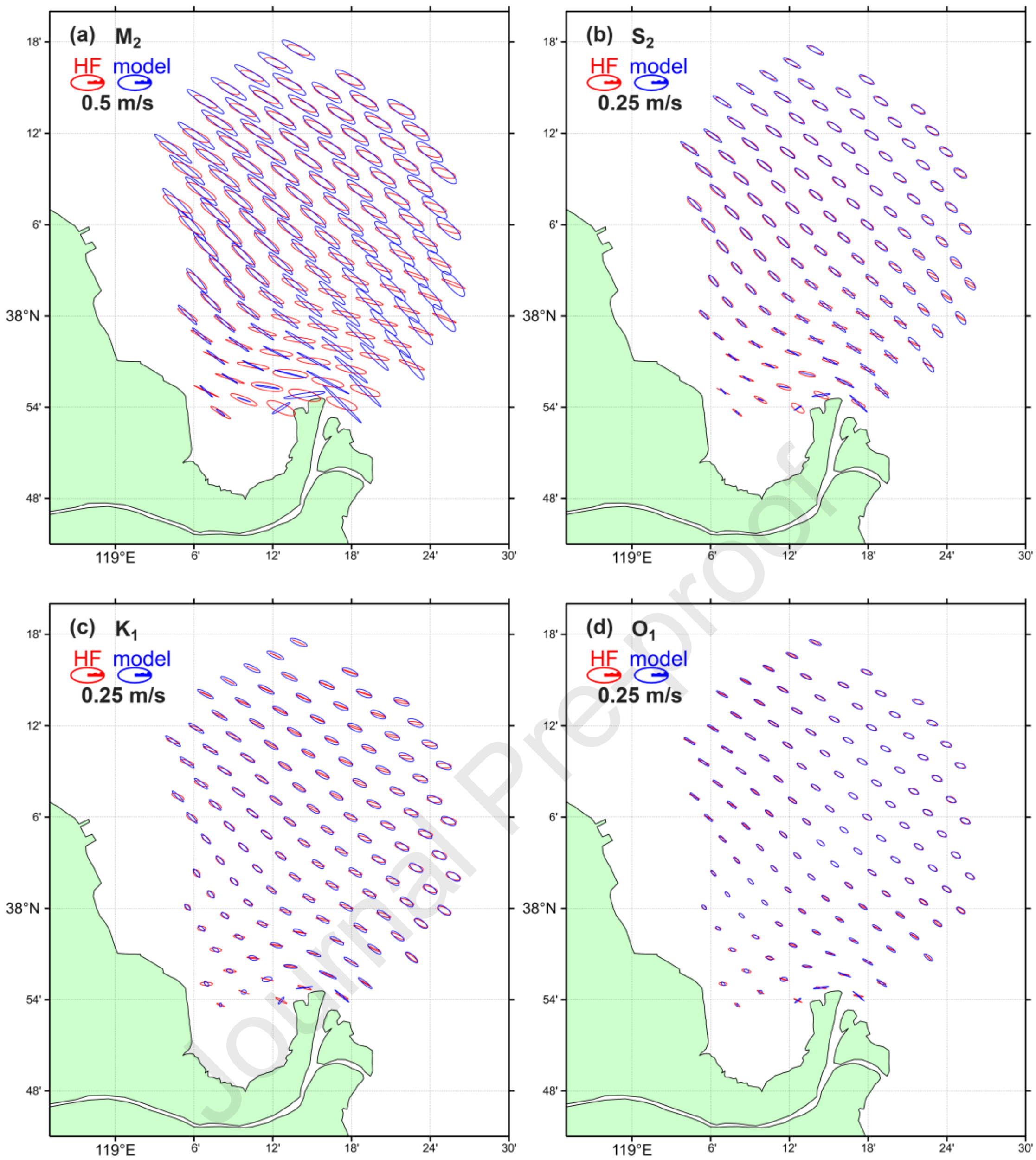

Figure 9. Distributions of tidal current ellipses for the four major tidal constituents derived from HFSWR (red ellipses) and the model (blue ellipses): (a) M_2, (b) S_2, (c) K_1, and (d) O_1.

To quantitatively assess the discrepancies between surface tidal currents observed by HFSWR and those simulated by the POM model (Yu et al., 2021), this study computed the averaged root mean square error (RMSE) using the following formula (Wang et al., 2021):

$$RMSE_u = \frac{1}{m}\sum_{1}^{m}\sqrt{\frac{1}{T}\int_{0}^{T}[u_o(t) - u_m(t)]^2 d\,t} \tag{2}$$

$$RMSE_v = \frac{1}{m}\sum_{1}^{m}\sqrt{\frac{1}{T}\int_{0}^{T}[v_o(t) - v_m(t)]^2 d\,t} \tag{3}$$

here, u and v denote the eastward and northward components of the tidal currents, respectively; m represents the number of valid grid points in the region; T corresponds to the period of the respective tidal constituent; the subscript $_o$ of u and v indicates radar observations, while $_m$ refers to model results. RMSEs calculated from Eqs. (2) – (3) are summarized in Table 2. Spatially averaged values for the u component are 0.18, 0.01, 0.12, and 0.05 m/s for M_2, S_2, K_1, and O_1, respectively; the corresponding values for v are 0.20, 0.02, 0.08, and 0.04 m/s. The spatial distribution of root-mean-square errors between radar observations and simulated M_2 tidal currents (Figure 10) revealed pronounced discrepancies in both u and v components in the vicinity of the Yellow River estuary. Both components exhibit RMSE exceeding 0.20 m/s (Figure 10a, b). These elevated errors near the Yellow River estuary likely originated from discrepancies between the model's bathymetric representation and actual geomorphic conditions. Although the model incorporated shoreline data from 2021, it utilized bathymetric data near Yellow River estuary from the sea chart in 2006 and did not account for the topography alternations due to continuous erosion and siltation near the Yellow River Delta over several decades. This bathymetric mismatch may introduce systematic biases in magnitudes and phase of the simulated tidal current near the Yellow River estuary.

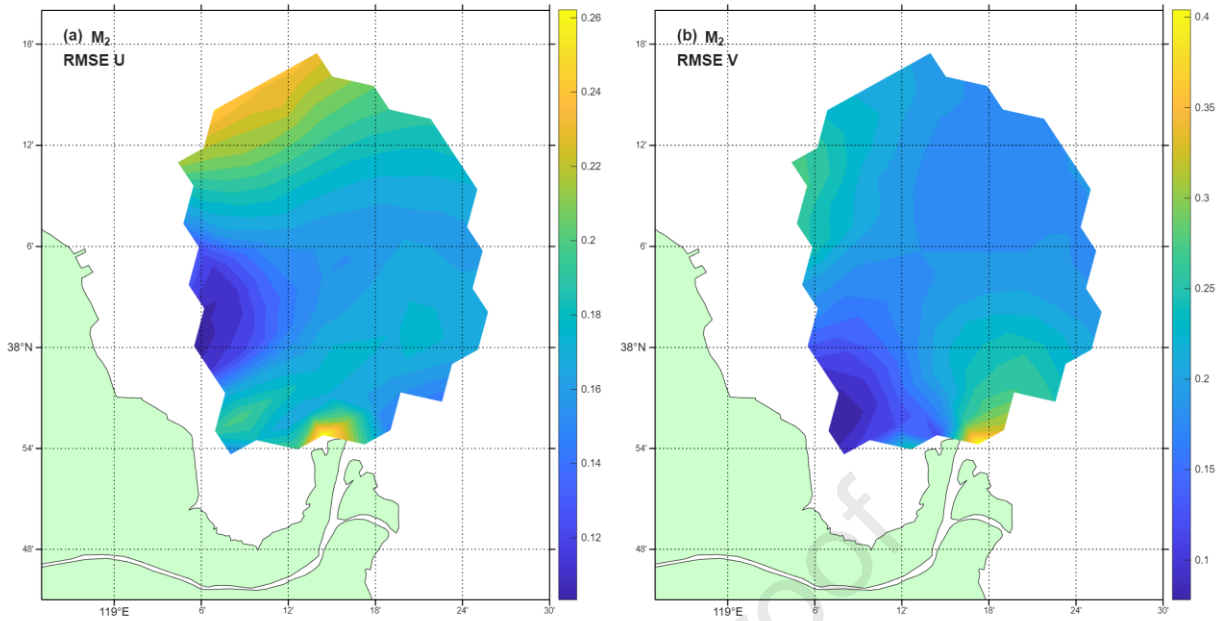

Figure 10. Root-mean-square errors (m/s) between radar observations and simulations of M_2 tidal current for (a) eastward component and (b) northward component.

Table 2. Statistical errors of the spatially averaged RMSE between HFSWR and the POM model for the four primary tidal constituents. Values are shown as mean ± spatial standard deviation.

Constituent	Mean $RMSE_U$ ± SD (m/s)	Mean $RMSE_V$ ± SD (m/s)
M_2	0.18 ± 0.03	0.20 ± 0.05
S_2	0.01 ± 0.01	0.02 ± 0.01
K_1	0.12 ± 0.02	0.08 ± 0.02
O_1	0.05 ± 0.01	0.04 ± 0.01

The HFSWR observations confirmed the existence of two strong tidal current zones north of the Yellow River estuary—one adjacent to the M_2 amphidromic point and the other near the estuary.

Besides, the tidal current near the Yellow River estuary was found to be rotational flow rather than rectilinear flow. Given the continuously evolving shoreline topography and bathymetry in the vicinity of the Yellow River estuary, as well as the challenges faced by existing high-resolution models in incorporating real-time topographic data, the application of HFSWR for observation and analysis in this region was of critical importance (Dumas et al., 2025). Such efforts are essential for enhancing model accuracy and deepening the understanding of the dynamic environment near the estuary.

4.2 The mechanism of the seasonal variation of tidal currents in the northern area of Yellow River estuary

The amplitude of the M_2 tidal current was notably large around the M_2 amphidromic point (near Shenxiangou) and near the Yellow River estuary as compared to other regions in all five months. This phenomenon could be attributed to distinct dynamic mechanisms. The M_2 amphidromic point near Shenxiangou acts as a node of a standing wave, where the flow velocity is largest. The strong tidal current zone near the Yellow River estuary was influenced by local bathymetric features, including seabed depressions, sediment cliffs, and steep slopes at the estuary front. The convergence effect induced by this complex topography enhanced the tidal current velocity as the tidal wave passed through (Prandle, 1997; Wang et al., 2015).

The observed seasonal modulation of M_2 tidal characteristics in these two areas is closely linked to the evolution of density stratification (Müller et al., 2014). Density stratification modifies tidal propagation through two distinct pathways, depending on water depth and topographic context (Müller, 2012; Opel et al., 2024). In deep water or over steep topography, a strengthened pycnocline facilitates barotropic-to-baroclinic energy conversion. This generates internal tides and subsequently decreases the energy for propagation of the barotropic tide (Garrett and Kunze, 2007; Opel et al., 2024). In shallow shelf seas and estuaries, however, stratification reduces eddy viscosity, thins the bottom boundary layer, and weakens bottom friction, thereby lessening the dissipation of barotropic tidal energy (Müller et al., 2014; Kang et al., 2002). Consequently, less barotropic tidal kinetic energy is lost to friction, allowing the tide to propagate with higher amplitude. The Yellow River estuary is a shallow water region, where stratification could strengthen the tidal energy through decreasing bottom friction. Theoretically, wind could influence tidal current characteristics by affecting vertical mixing and stratification. However, previous studies indicate that the effect of wind on stratification is relatively small in the Bohai Sea (Huang et al., 1999), and that tidal mixing, rather than wind, dominates vertical mixing in summer (Ma et al., 2017). Specifically, near the Yellow River estuary, the large summer river discharge (~4000 m^3/s) establishes strong density stratification, which could not be broken by the weak summer wind (Figure 2).

To quantitatively analyze the influence of density stratification on the seasonal variability of tidal currents, the Brunt-Väisälä frequency (N^2), a measure of buoyancy frequency, is used, which is defined as:

$$N^2 = -\frac{g}{\rho}\frac{\partial \rho}{\partial z} \tag{4}$$

herein, ρ denotes seawater density, g represents gravitational acceleration, z indicates depth within the water column, $\frac{\partial \rho}{\partial z}$ refers to the vertical seawater density gradient. The vertical density gradient was first computed at measurement depths using central differences (one-sided at the boundaries). N^2 was then evaluated at the mid-points between adjacent measured levels, with both density and gradient taken as the arithmetic means of the two adjacent values. As defined by the above equation, the squared Brunt-Väisälä frequency serves as an indicator of stratification strength:

generally, higher values signify stronger stratification, while lower values signify weaker stratification.

The in-situ measurements of water temperature and salinity from the three surveys conducted in May, June, and July 2022 were used to examine the temporal change in density stratification intensity within the study area. Although the year of these field campaigns is different from that of radar observation, the observations for water temperature and salinity represent the seasonal variations. Observational data at two selected stations (P1 and P2 in Figure 1c) were specifically analyzed—with P1 near Shenxiangou, and P2 near the Yellow River estuary—to investigate the seasonal variation of density stratification in the northern Yellow River estuary coastal waters.

Figure 11 illustrates the vertical variation of the Brunt-Väisälä frequency squared (N^2) at P1 and P2. At P1 (Figure 11a), the N^2 value was minimal in May ($< 1.0 \times 10^{-4}$ s^{-2}), indicating a nearly well-mixed water column. However, in June and July, the N^2 values increased significantly (maximum about 7.7×10^{-4}~8.3×10^{-4} s^{-2}), reflecting a strengthening of stratification from spring to summer. At P2 (Figure 11b), the N^2 values were lower in May and June ($< 4.2 \times 10^{-3}$ s^{-2}), while it increased largely in July ($> 8.0 \times 10^{-3}$ s^{-2}). Consistent with this seasonal intensification of stratification, the tidal current amplitude at both P1 and P2 also showed an increasing trend during the corresponding seasonal period. A broadly similar seasonal pattern was observed in the radar-derived surface tidal amplitude, which increased markedly near the Yellow River estuary in Period 4 (Figure 7d). The lack of field data in August and September precludes direct comparison for those months, but the established seasonal relationship supports a similar expectation. The consistent seasonal association between stratification intensification and surface tidal amplitude enhancement suggests that stratification may play an important role in influencing the seasonal variation of surface tidal currents in the northern region of the Yellow River estuary.

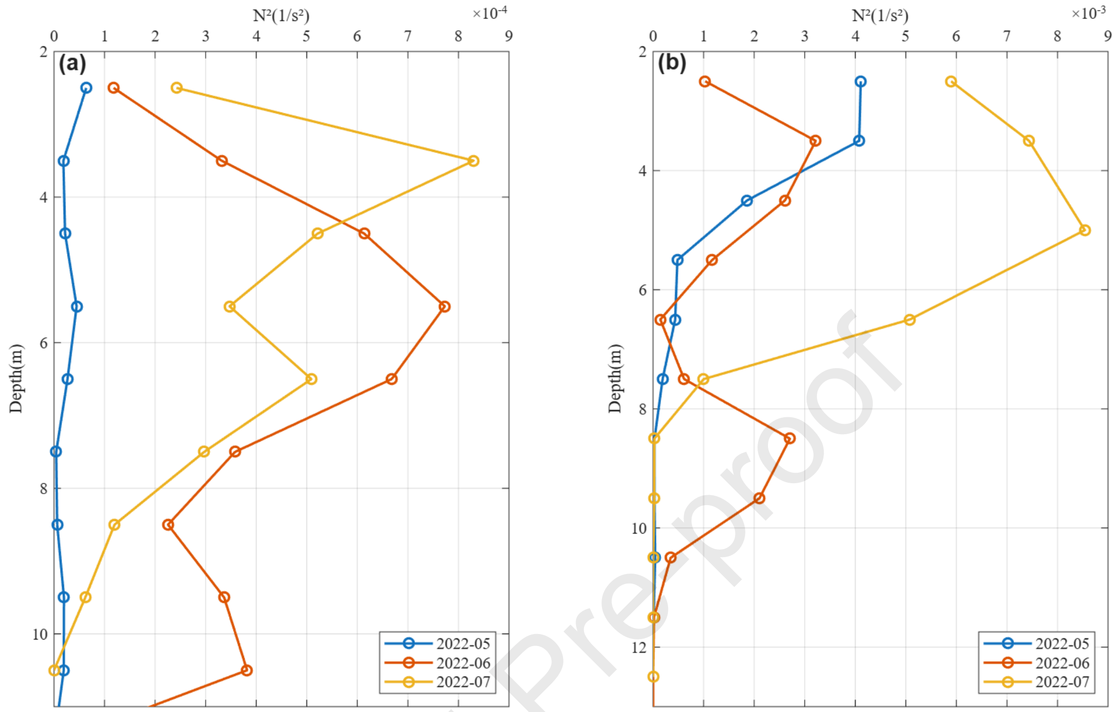

Figure 11. Variations of Brunt–Väisälä frequency squared (N^2) with water depth at (a) Point P1 and (b) Point P2. Point locations are shown in Figure 1c.

To further assess the relative contributions of temperature and salinity to density stratification, we calculated the density ratio:

$$R\rho = \frac{|\alpha(\partial T/\partial z)|}{|\beta(\partial S/\partial z)|} \quad (5)$$

where α is the thermal expansion coefficient, β is the saline contraction coefficient, ∂T/∂z and ∂S/∂z are the vertical gradients of temperature and salinity, respectively. R_ρ represents the absolute ratio of thermal to haline contributions on stratification, with value below 1 indicating salinity-dominated stratification, while value above 1 indicating temperature-dominated stratification. The vertical distribution of R_ρ at both stations is shown in Figure 12. At site P1, most values across the 2–11 m depth were below 1, with only two depths as exceptions. Specifically, R_ρ reached 63.05 at 2m in

May, which was attributed to a near-zero salinity gradient and therefore excluded from further analysis. Elevated R_ρ values (>1) were observed at 4 m in May and at 4 m and 10 m in July, signifying that temperature exerted a dominant control on density variations at these depths. At site P2, almost every measured depth in May, June, and July yielded R_ρ values below 1. The consistently sub-unit R_ρ throughout the water column demonstrates that salinity gradients dominated the local density stratification during the entire study period. At P1, temperature made an additional but lesser contribution, while at P2, stratification was almost entirely controlled by salinity. Consequently, it can be inferred that during the observation period, increased stratification in the Shenxiangou and Yellow River estuary regions was chiefly governed by vertical salinity gradients induced by increased Yellow River discharge. This increased salinity-driven stratification led to significant seasonal fluctuations in the amplitude of the M_2 tidal constituent within the two areas.

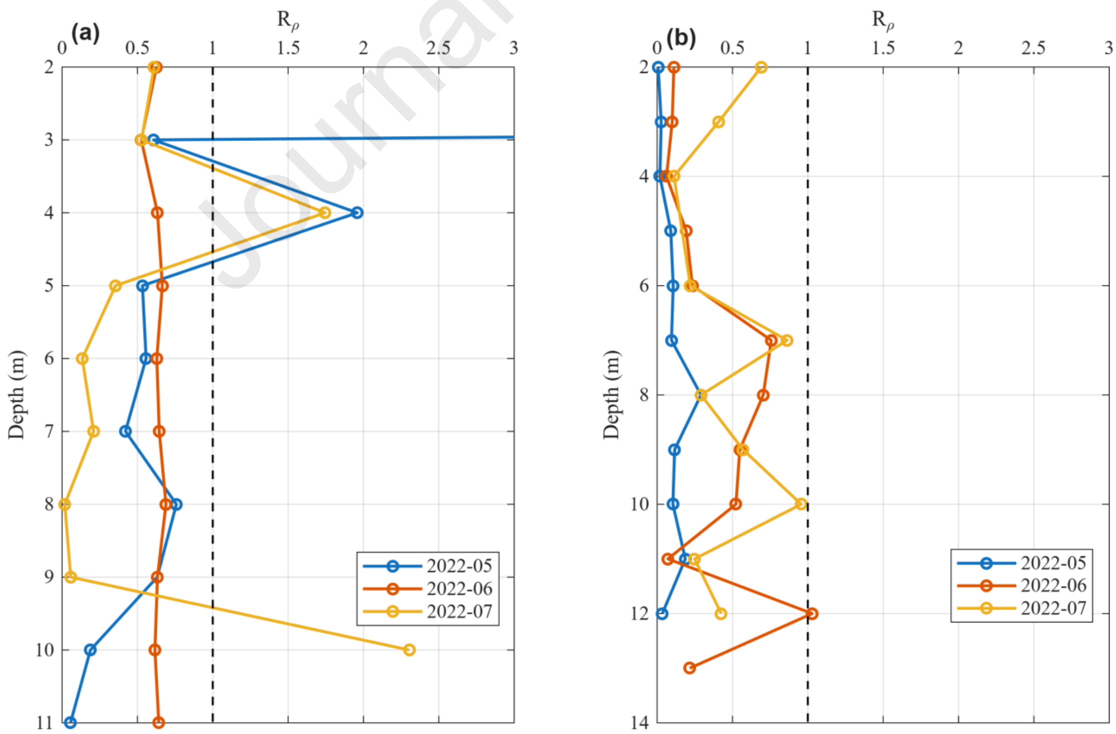

Figure 12. Vertical profiles of density ratio (R_ρ) at stations (a) P1 and (b) P2 during May (blue), June (red), and July (yellow) 2022. The dashed line at $R_\rho = 1$ indicates equal contributions from temperature and salinity on density stratification.

From spring to summer, the ellipticity of M_2 tidal current also increased, indicating clockwise rotational intensification near the Yellow River estuary and northern area. This phenomenon may also be closely associated with density stratification. Next, we will discuss the influence of stratification on the variation of the ellipticity of tidal current ellipses based on the properties of boundary layer theory. Typically, tidal currents characterized by elliptical trajectories can be effectively decomposed into clockwise and counterclockwise components. According to Prandle (1982), the characteristic boundary layer thicknesses for these two motion components are expressed as follows:

$$\delta_{\pm} \approx \left(\frac{2N_z}{(\omega \pm f)}\right)^{\frac{1}{2}} \tag{6}$$

where δ_- and δ_+ correspond to boundary layer thicknesses associated with clockwise and counterclockwise motions, respectively; N_z characterizes eddy viscosity, ω indicates tidal frequency (1.4×10^{-4}/s for M_2), f represents the Coriolis parameter (8.98×10^{-5}/s at 38°N). Wang et al. (2011) demonstrated that under vertically well-mixed conditions, the clockwise component's bottom boundary layer near the Yellow River estuary could encompass the entire water column, while the counterclockwise component's bottom boundary layer is small. They further noted that the stable stratification reduced N_z (eddy viscosity) near the pycnocline, consequently decreasing δ_- (boundary layer thickness). It then confined bottom frictional effects to a thinner near-bed region and conserved momentum in the surface layer, which directly amplify the clockwise component of surface tidal current (Souza and Simpson, 1996). For the M_2 tidal constituent in the Yellow River estuary, the clockwise rotating component exceeds the counterclockwise counterpart (Figure 4); thus, the amplification of this dominant clockwise component directly increases the ellipticity of the tidal ellipse (Pugh, 1987; Souza and Simpson, 1996; Carbajal and Pohlmann, 2004).

To quantitatively assess this mechanism, we estimated the boundary layer thickness at stations P1 and P2. Under well-mixed conditions, we set $N_z = N_0$, which is computed using the following formula:

$$N_0 = \frac{1}{2} k_b U H \tag{7}$$

where k_b represents the effective bottom drag coefficient (0.0015, Guo and Yanagi, 1998), U denotes the tidal current amplitude, and H indicates the water depth. Under stratified conditions, stratification effects were incorporated through the Munk and Anderson (1948) correction:

$$N_z = N_0 (1 + 10Ri)^{-1/2} \tag{8}$$

herein $Ri = \frac{N^2 H^2}{U^2}$ is the bulk Richardson number, in which N^2 is the Brunt-Väisälä frequency in Eq. (4). To represent the strongest stratification suppression on vertical mixing, N^2 was taken as the peak value within the pycnocline. Substituting N_z into Eq. (6) yields the boundary layer thickness.

At P1 (H = 12 m), Ri increased from 0.08 in May to 0.47–0.50 in June－July as stratification developed. Consequently, δ_- decreased from 12.2 m in May to ~8.6 m in June－July. In May, under well-mixed conditions, δ_- exceeded the water depth, indicating that bottom friction influenced the entire water column. As stratification intensified in June－July, δ_- was ~8.6 m, thinner than the water depth, partially decoupling surface currents from bottom friction. At P2 (H = 14 m), Ri remained above 3.6 throughout the study period, and δ_- was only 4.5 m in May and further decreased to 4.3 m in July. The boundary layer was always much thinner than the water depth. This indicates that bottom friction was confined to the lower layer and surface currents were largely decoupled from bottom flows. From May to July, the boundary layer gradually became thinner, corresponding with the ongoing increase in clockwise ellipticity, meaning a greater degree of ellipticity.

Notably, an increase in tidal current ellipticity from spring to summer was also observed in the northeastern area beyond the estuarine zone (Figure 8). Although direct observational data on stratification conditions are unavailable here, numerical modeling results have revealed a clear intensification of thermal stratification in this area during summer (Wang et al., 2008). With the same mechanism, it can be inferred that the amplification of the clockwise tidal current component caused by enhanced stratification is responsible for the increase in tidal ellipse ellipticity in the northeastern area.

5. Conclusions

This study used high-frequency surface wave radar (HFSWR) to investigate surface tidal currents in the northern Yellow River estuary. Compared to previous point-based measurements, HFSWR provided unprecedented spatial and temporal resolution. It revealed a predominantly semidiurnal tidal regime with M_2 dominating. Two distinct M_2 strong-flow zones near Shenxiangou (a standing tidal wave node) and near the estuary were resolved. Notably, high-resolution mapping confirmed that M_2 ellipses near the estuary exhibited rotational flow. This resolves the long-standing debate and challenges the traditional view of purely back-and-forth oscillatory flow in this region.

Marked seasonal variations in M_2 ellipses occurred, driven by time-varying stratification. Stratification near Shenxiangou was jointly influenced by water warming and salinity changes, with the latter appearing to contribute more. Stratification near the estuary was mainly attributed to the vertical salinity gradient from increased river discharge. These time-varying stratification conditions significantly modulated surface tidal currents. Specifically, intensified stratification tended to suppress the vertical dissipation of tidal kinetic energy, thereby increasing surface M_2 amplitudes. Furthermore, stratification near the estuary likely reduced the eddy viscosity coefficient and thinned the boundary layer of the clockwise-rotating component. This generally enhanced the clockwise rotation of M_2 ellipses during maximum river discharge, explaining seasonal changes in ellipticity near the river mouth.

Several limitations should also be acknowledged. The observation period spans only from April to September, lacking data from autumn and winter, which limits a full characterization of the annual variability of tidal currents. Moreover, the HF radar data are confined to the surface layer, so the vertical structure of tidal currents cannot be resolved. Additionally, although strong winds and associated surface waves may affect radar measurements, wind conditions were generally moderate during the observation period, and the influence of wave interference is considered limited.

Acknowledgments. This study was funded by the National Natural Science Foundation of China (42276010; 42149301, NORC2022-304). Y. Wang was supported by Study on big data assimilation and fusion analysis model of super-resolution marine environment funded by the National Key Research and Development Program of China (No. 2021YFF0704002). X. Guo was supported by a Grant-in-Aid for Scientific Research (MEXT KAKENHI, grant number: 22H05206). This study was also partly supported by the Ministry of Education, Culture, Sports, Science and Technology, Japan (MEXT) to a project on Joint Usage/Research Center–Leading Academia in

Marine and Environment Pollution Research (Lamer).

Reference

Atlas, R., Hoffman, R. N., Ardizzone, J., Leidner, S. M., Jusem, J. C., Smith, D. K., & Gombos, D. (2011). A Cross-calibrated, Multiplatform Ocean Surface Wind Velocity Product for Meteorological and Oceanographic Applications. *Bulletin of the American Meteorological Society*, *92*(2), 157–174. https://doi.org/10.1175/2010BAMS2946.1

Bi, N., Yang, Z., Wang, H., Hu, B., & Ji, Y. (2010). Sediment dispersion pattern off the present Huanghe (Yellow River) subdelta and its dynamic mechanism during normal river discharge period. *Estuarine, Coastal and Shelf Science*, *86*(3), 352–362. https://doi.org/10.1016/j.ecss.2009.06.005

Blumberg, A. F., & Mellor, G. L. (1987). A Description of a Three-Dimensional Coastal Ocean Circulation Model. *In Three-Dimensional Coastal Ocean Models, N.S. Heaps (Ed.)*. https://doi.org/10.1029/CO004p0001

Cancet, M., Griffin, D., Cahill, M., Chapron, B., Johannessen, J., & Donlon, C. (2019). Evaluation of GlobCurrent surface ocean current products: A case study in Australia. *Remote Sensing of Environment*, *220*, 71–93. https://doi.org/10.1016/j.rse.2018.10.029

Carbajal, N., & Pohlmann, T. (2004). Comparison between measured and calculated tidal ellipses in the German Bight. *Ocean Dynamics*, *54*(5), 520–530. https://doi.org/10.1007/s10236-004-0096-5

Chapman, R. D., Shay, L. K., Graber, H. C., Edson, J. B., Karachintsev, A., Trump, C. L., & Ross, D. B. (1997). On the accuracy of HF radar surface current measurements: Intercomparisons with ship-based sensors. *Journal of Geophysical Research: Oceans*, *102*(C8), 18737–18748. https://doi.org/10.1029/97JC00049

Chavanne, C., Janeković, I., Flament, P., Poulain, P. -M., Kuzmić, M., & Gurgel, K. -W. (2007). Tidal currents in the northwestern Adriatic: High-frequency radio observations and numerical model predictions. *Journal of Geophysical Research: Oceans*, *112*(C3), 2006JC003523. https://doi.org/10.1029/2006JC003523

Dumas, D., Bennis, A.-C., Guérin, C.-A., Lopez, G., & Benoit, L. (2025). High-Frequency Radar observation of strong and sheared currents: The Alderney race paradigm. *Ocean Dynamics*, *75*(6), 45. https://doi.org/10.1007/s10236-025-01689-0

Fang, G. (1994). Tides and Tidal Currents in East China Sea, Huanghai Sea and Bohai Sea. In: Z. Di, L. Yuan-Bo, & Z. Cheng-Kui (Eds.), *Oceanology of China Seas* (pp. 101–112). Springer Netherlands. https://doi.org/10.1007/978-94-011-0862-1_11

Gao, J., Chen, X., Yu, H., & Li, M. (2016). Numerical simulation of tides, tidal currents and residual currents in the Yellow River estuary. *Marine Science Bulletin*, *18*(1), 1–8.

Garrett, C., & Kunze, E. (2007). Internal Tide Generation in the Deep Ocean. *Annual Review of Fluid Mechanics*, *39*, 57–87. https://doi.org/10.1146/annurev.fluid.39.050905.110227

Guo, D., Kartadikaria, A., Zhan, P., Xie, J., Li, M., & Hoteit, I. (2018). Baroclinic Tides Simulation in the Red Sea: Comparison to Observations and Basic Characteristics. *Journal of Geophysical Research: Oceans*, *123*(12), 9389–9404. https://doi.org/10.1029/2018JC013970

Guo, X., & Yanagi, T. (1998). Three-dimensional structure of tidal current in the East China Sea and the Yellow Sea. *Journal of Oceanography*, *54*(6), 651–668. https://doi.org/10.1007/BF02823285

Hsu, P.-C., Centurioni, L., Shao, H.-J., Zheng, Q., Lu, C.-Y., Hsu, T.-W., & Tseng, R.-S. (2021). Surface Current Variations and Oceanic Fronts in the Southern East China Sea: Drifter Experiments, Coastal Radar Applications, and Satellite Observations. *Journal of Geophysical Research: Oceans*, *126*(10), e2021JC017373. https://doi.org/10.1029/2021JC017373

Huang, D., Su, J., & Backhaus, J. O. (1999). Modelling the seasonal thermal stratification and baroclinic circulation in the Bohai Sea. *Continental Shelf Research*, *19*(11), 1485–1505. https://doi.org/10.1016/S0278-4343(99)00026-6

Kang, S. K., Foreman, M. G. G., Lie, H.-J., Lee, J.-H., Cherniawsky, J., & Yum, K.-D. (2002). Two-layer tidal modeling of the Yellow and East China Seas with application to seasonal variability of the M2 tide. *Journal of Geophysical Research: Oceans*, *107*(C3), 6-1–6-18. https://doi.org/10.1029/2001JC000838

Kaplan, D. M., Largier, J., & Botsford, L. W. (2005). HF radar observations of surface circulation off Bodega Bay (northern California, USA). *Journal of Geophysical Research: Oceans*, *110*(C10), 2005JC002959. https://doi.org/10.1029/2005JC002959

Lai, Y., Zhou, H., & Wen, B. (2017). Surface Current Characteristics in the Taiwan Strait Observed by High-Frequency Radars. *IEEE Journal of Oceanic Engineering*, *42*(2), 449–457. https://doi.org/10.1109/JOE.2016.2572818

Lee, S.-H., Kang, C.-Y., Choi, B.-J., & Kim, C.-S. (2013). Surface current response to wind and plumes in a bay-shape estuary of the eastern Yellow Sea: Ocean radar observation. *Ocean Science Journal*, *48*(1), 117–139. https://doi.org/10.1007/s12601-013-0010-5

Lipa, B. J., Barrick, D. E., Isaacson, J., & Lilleboe, P. M. (1990). CODAR wave measurements from a North Sea semisubmersible. *IEEE Journal of Oceanic Engineering*, *15*(2), 119–125. https://doi.org/10.1109/48.50697

Ma, W., Wan, X., Wang, Z., Liu, Y., & Wan, K. (2017). Formation of well-mixed warm water column in central Bohai Sea during summer: Role of high-frequency atmospheric forcing. *Journal of Ocean*

University of China, *16*(6), 945–952. https://doi.org/10.1007/s11802-017-3251-6

Mandal, S. (2024). Observed seasonality of M_2 and M_4 tidal currents in the Gulf of Khambhat using high-frequency radars. *Ocean Dynamics*, *74*(3), 251–265. https://doi.org/10.1007/s10236-024-01601-2

Mellor, G. L., & Yamada, T. (1982). Development of a turbulence closure model for geophysical fluid problems. *Reviews of Geophysics*, *20*(4), 851–875. https://doi.org/10.1029/RG020i004p00851

Müller, M. (2012). The influence of changing stratification conditions on barotropic tidal transport and its implications for seasonal and secular changes of tides. *Continental Shelf Research*, *47*, 107～118. https://doi.org/10.1016/j.csr.2012.07.003

Müller, M., Cherniawsky, J. Y., Foreman, M. G. G., & von Storch, J.-S. (2014). Seasonal variation of the M2 tide. *Ocean Dynamics*, *64*(2), 159–177. https://doi.org/10.1007/s10236-013-0679-0

Munk, W., & Anderson, E. (1948). Notes on a theory of the thermocline. *Journal of Marine Research*, *7*(3), 276–295.https://elischolar.library.yale.edu/journal_of_marine_research/667

Opel, L., Schindelegger, M., & Ray, R. D. (2024). A likely role for stratification in long-term changes of the global ocean tides. *Communications Earth & Environment*, *5*(1), 261. https://doi.org/10.1038/s43247-024-01432-5

Paduan, J. D., & Washburn, L. (2013). High-Frequency Radar Observations of Ocean Surface Currents. *Annual Review of Marine Science*, *5*(1), 115–136. https://doi.org/10.1146/annurev-marine-121211-172315

Pang, J. Z., & Jiang, M. X. (2003). On the evolution of the Yellow River estuary (I): I. Hydrographic characteristics. Transactions of Oceanology and Limnology, 3, 1-13.

Pawlowicz, R., Beardsley, B., & Lentz, S. (2002). Classical tidal harmonic analysis including error estimates in MATLAB using T_TIDE. *Computers & Geosciences*, *28*(8), 929–937. https://doi.org/10.1016/S0098-3004(02)00013-4

Pugh, D. T. (1987). Tides, surges and mean sea level. John Wiley & Sons.

Prandle, D. (1982). The vertical structure of tidal currents and other oscillatory flows. *Continental Shelf Research*, *1*(2), 191–207. https://doi.org/10.1016/0278-4343(82)90004-8

Prandle, D. (1997). Tidal currents in shelf seas—Their nature and impacts. *Progress in Oceanography*, *40*(1–4), 245–261. https://doi.org/10.1016/S0079-6611(98)00013-5

Schneider, D. P., Deser, C., Fasullo, J., & Trenberth, K. E. (2013). Climate Data Guide Spurs Discovery and Understanding. *Eos, Transactions American Geophysical Union*, *94*(13), 121–122. https://doi.org/10.1002/2013EO130001

Shen, Z., Wu, X., Fei, Y., Xu, X., & Chen, X. (2013). Surface tidal currents in the open sea area to the east of the Zhoushan Islands measured with high frequency surface wave radar. *Acta Oceanologica Sinica*, *32*(10), 5–10. https://doi.org/10.1007/s13131-013-0359-4

Shen, Z., Wu, X., Lin, H., Chen, X., Xu, X., & Li, L. (2014). Spatial distribution characteristics of surface tidal currents in the southwest of Taiwan Strait. *Journal of Ocean University of China*, *13*(6), 971–978. https://doi.org/10.1007/s11802-014-2314-1

Smagorinsky, J. (1963). GENERAL CIRCULATION EXPERIMENTS WITH THE PRIMITIVE EQUATIONS: I. THE BASIC EXPERIMENT. *Monthly Weather Review*, *91*(3), 99–164. https://doi.org/10.1175/1520-0493(1963)091%253C0099:GCEWTP%253E2.3.CO;2

Souza, A. J., & Simpson, J. H. (1996). The modification of tidal ellipses by stratification in the Rhine ROFI. *Continental Shelf Research*, *16*(8), 997–1007. https://doi.org/10.1016/0278-4343(95)00042-

9

Wang, C., Tian, Y., Yang, J., Zhou, H., Wen, B., Xu, X., & Huang, W. (2020). Validation and Intercomparison of Sea State Parameter Estimation With Multisensors for OSMAR-S High-Frequency Radar. *IEEE Transactions on Instrumentation and Measurement*, *69*(10), 7552–7565. https://doi.org/10.1109/TIM.2020.2986101

Wang, L., Pawlowicz, R., Wu, X., & Yue, X. (2021). Wintertime Variability of Currents in the Southwestern Taiwan Strait. *Journal of Geophysical Research: Oceans*, *126*(5), e2020JC016586. https://doi.org/10.1029/2020JC016586

Wang, N., Li, G., Xu, J., Qiao, L., Dada, O. A., & Zhou, C. (2015). The marine dynamics and changing trend off the modern Yellow River mouth. *Journal of Ocean University of China*, *14*(3), 433–445. https://doi.org/10.1007/s11802-015-2764-0

Wang, Q., Guo, X., & Takeoka, H. (2008). Seasonal variations of the Yellow River plume in the Bohai Sea: A model study. *Journal of Geophysical Research: Oceans*, *113*(C8), 2007JC004555. https://doi.org/10.1029/2007JC004555

Wang, Y., Liu, Z., Gao, H., Ju, L., & Guo, X. (2011). Response of salinity distribution around the Yellow River mouth to abrupt changes in river discharge. *Continental Shelf Research*, *31*(6), 685–694. https://doi.org/10.1016/j.csr.2011.01.005

Wang, Y., Zhou, Z., Cao, B., & Ge, J. (2025). Shifting Dynamics for Coastal Upwelling and Surface Cold Water Patch: A Synergy of HF-Radar, In-Site Observation, Satellite, and Numerical Model. *IEEE Transactions on Geoscience and Remote Sensing*, *63*, 1–13. https://doi.org/10.1109/TGRS.2025.3559935

Wang, Z., Drevillon, M., De Mey-Frémaux, P., Remy, E., Ayoub, N., Wang, D., & Levier, B. (2024).

High frequency radar error classification and prediction based on K-means methods. *Frontiers in Marine Science*, *11*. https://doi.org/10.3389/fmars.2024.1448427

Wiseman, W. J., Fan, Y.-B., Bornhold, B. D., Keller, G. H., Su, Z.-Q., Prior, D. B., Yu, Z.-X., Wright, L. D., Wang, F.-Q., & Qian, Q.-Y. (1986). Suspended sediment advection by tidal currents off the Huanghe (Yellow River) delta. *Geo-Marine Letters*, *6*(2), Article 2. https://doi.org/10.1007/BF02281646

Wu, D., Yu, X., Guo, X., Wang, Y., Gao, H., Zou, T., & Tang, J. (2025). Delay effect of Yellow River discharge on the water exchange through the Bohai Strait. Frontiers in Marine Science, 12. https://doi.org/10.3389/fmars.2025.1512318

Xing, J., & Davies, A. M. (1998). Influence of Stratification upon Diurnal Tidal Currents in Shelf Edge Regions. *Journal of Physical Oceanography*, *28*(9), 1803-1831. https://doi.org/10.1175/1520-0485(1998)028<1803:IOSUDT>2.0.CO;2

Yu, X., Guo, X., & Gao, H. (2020). Detachment of Low-Salinity Water From the Yellow River Plume in Summer. *Journal of Geophysical Research: Oceans*, *125*(10), e2020JC016344. https://doi.org/10.1029/2020JC016344

Yu, X., Guo, X., Gao, H., & Zou, T. (2021). Upstream extension of a bottom-advected plume and its mechanism: The case of the Yellow River. *Journal of Physical Oceanography*, *51*(7), 2351–2371. https://doi.org/10.1175/JPO-D-20-0235.1

Zaron, E. D., & Elipot, S. (2024). Estimates of Baroclinic Tidal Sea Level and Currents from Lagrangian Drifters and Satellite Altimetry. *Journal of Atmospheric and Oceanic Technology*, *41*(8), 781–802. https://doi.org/10.1175/JTECH-D-23-0159.1

Zhang, L., Shi, H., Xing, H., Li, P., & Ma, P. (2023). Analysis of the evolution of the Yellow River Delta coastline and the response of the tidal current field. *Frontiers in Marine Science*, *10*, 1232060. https://doi.org/10.3389/fmars.2023.1232060

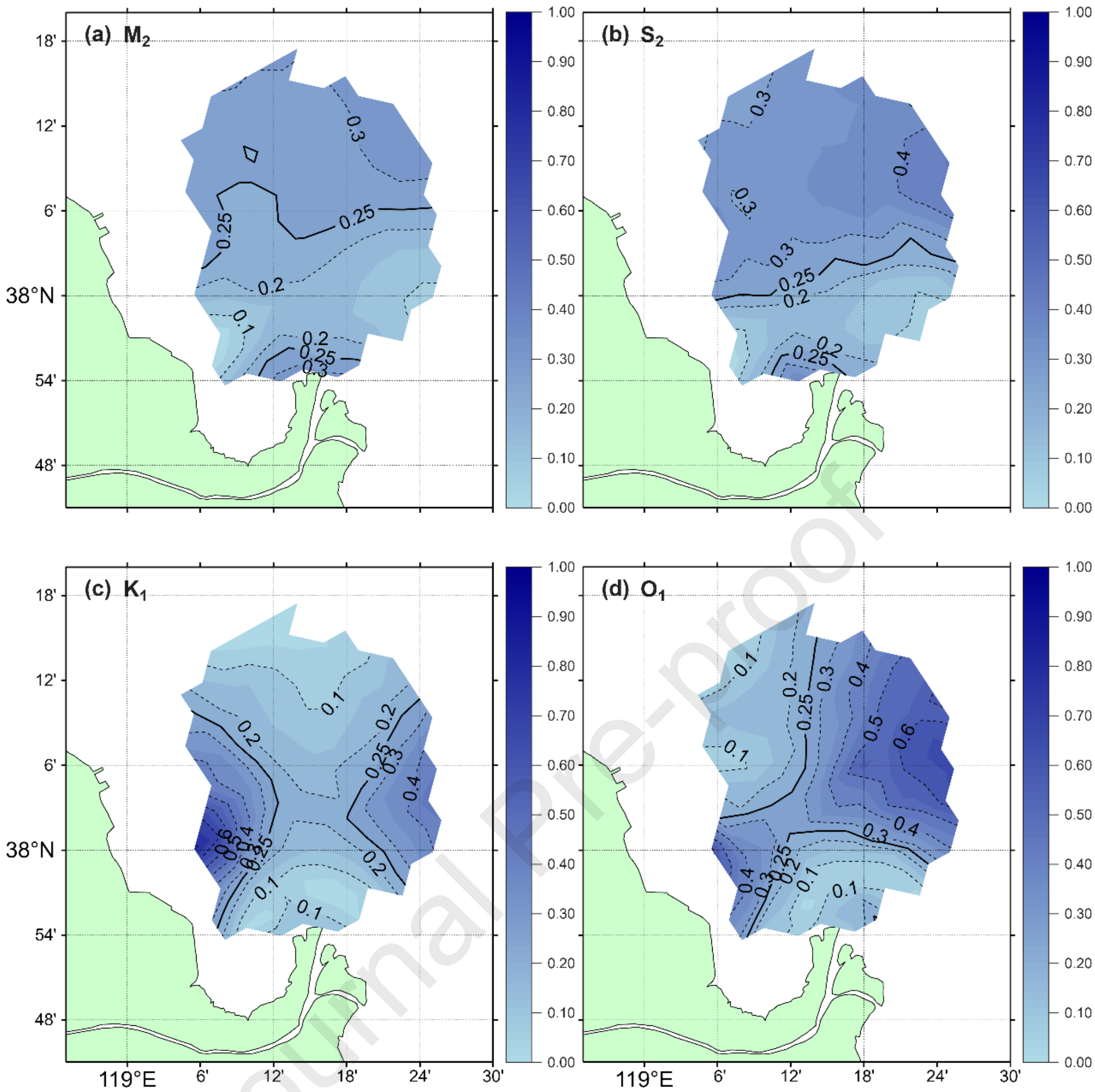
(a) M2
(b) S2
(c) K1
(d) O1
18'
12'
6'
38°N
54'
48'
119°E
6'
12'
18'
24'
30'
1.00
0.90
0.80
0.70
0.60
0.50
0.40
0.30
0.20
0.10
0.00

- Two distinct M_2 strong-flow zones near the Yellow River estuary are delineated.
- M_2 tidal currents near estuary exhibit rotational motion rather than linear flow.
- Seasonal variations in M_2 amplitude are due to changes in density stratification.
- In estuarine region, stratification has the potential to enhance tidal ellipticity.

Declaration of interests

☒ The authors declare that they have no known competing financial interests or personal relationships that could have appeared to influence the work reported in this paper.

☐ The authors declare the following financial interests/personal relationships which may be considered as potential competing interests: